

Superconducting diode effect and interference patterns in Kagome CsV₃Sb₅

Tian Le,^{1,2,*} Zhiming Pan,^{1,2,3,*} Zhuokai Xu,^{1,2} Jinjin Liu,^{4,5} Jialu Wang,^{1,2} Zhefeng Lou,^{1,2} Xiaohui Yang,^{1,2,6} Zhiwei Wang,^{4,5,7,†} Yugui Yao,^{4,5,7} Congjun Wu,^{1,2,3,8,‡} and Xiao Lin^{1,2,§}

¹Key Laboratory for Quantum Materials of Zhejiang Province, Department of Physics, School of Science and Research Center for Industries of the Future, Westlake University, Hangzhou 310030, P. R. China

²Institute of Natural Sciences, Westlake Institute for Advanced Study, Hangzhou 310024, P. R. China

³Institute for Theoretical Sciences, Westlake University, 310024, Hangzhou, China

⁴Centre for Quantum Physics, Key Laboratory of Advanced Optoelectronic Quantum Architecture and Measurement (MOE), School of Physics, Beijing Institute of Technology, Beijing 100081, China

⁵Beijing Key Lab of Nanophotonics and Ultrafine Optoelectronic Systems, Beijing Institute of Technology, Beijing 100081, China

⁶Department of Physics, China Jiliang University, Hangzhou 310018, Zhejiang, P. R. China

⁷Material Science Center, Yangtze Delta Region Academy of Beijing Institute of Technology, Jiaxing 314011, China

⁸New Cornerstone Science Laboratory, Department of Physics, School of Science, Westlake University, 310024, Hangzhou, China

(Dated: May 17, 2024)

The interplay among frustrated lattice geometry, nontrivial band topology and correlation yields rich quantum states of matter in Kagome systems^{1,2}. A series of recent members in this family, AV₃Sb₅ (A= K, Rb, Cs), exhibit a cascade of symmetry-breaking transitions³, involving the 3Q chiral charge ordering⁴⁻⁸, electronic nematicity^{9,10}, roton pair-density-wave¹¹ and superconductivity¹². The nature of the superconducting order is yet to be resolved. Here, we report an indication of chiral superconducting domains with boundary supercurrents in intrinsic CsV₃Sb₅ flakes. Magnetic field-free superconducting diode effect is observed with polarity modulated by thermal histories, suggesting dynamical superconducting order domains in a spontaneous time-reversal symmetry breaking background. Strikingly, the critical current exhibits the double-slit superconducting interference patterns when subjected to an external magnetic field. Characteristics of the patterns are modulated by thermal cycling. These phenomena are proposed as a consequence of periodically modulated supercurrents flowing along certain domain boundaries constrained by fluxoid quantization. Our results imply a chiral superconducting order, opening a potential for exploring exotic physics, e.g. Majorana zero modes, in this intriguing topological Kagome system.

Chiral superconductors (SC), characterized by complex order parameters, break time-reversal symmetry (TRS) spontaneously. Certain types of chiral SCs are topologically non-trivial whose gap functions exhibit phase winding over the Fermi surface. They allow for exploring chiral edge states and Majorana zero modes, showing a promise for fault-tolerant topological quantum computation¹³. A well-known example exhibiting chiral pairing symmetry is the superfluid ³He-A phase¹⁴. In electronic materials, evidence of TRS breaking has been reported¹⁵⁻¹⁸, including Sr₂RuO₄¹⁵, UPt₃¹⁶ and UTe₂¹⁷. Nevertheless, an unequivocal demonstration of chiral edge supercurrent (I_e) at SC domain boundaries is still a pending target.

AV₃Sb₅ (A=K, Rb, Cs) exhibit a rich phase diagram featured by the intricate interplay among multiple intertwined orders^{4-11,19}. This hints the possibility of unconventional SC^{7,11,20}, yet the pairing symmetry remains unclear²¹⁻²⁷. Accumulated evidence²³⁻²⁷, including nuclear quadrupole resonance²³, tunnel diode oscil-

lator²⁴, electron irradiation²⁵ and angle-resolved photoemission spectroscopy²⁶, surprisingly indicates the presence of nodeless, spin-singlet, and nearly isotropic SC gaps. From a theoretical perspective, a chiral SC state with a fully gapped composite gap function has been proposed in literature²⁸⁻³⁰. Relevant clues to this are elusive^{6,22,26,31}, derived exclusively from muon spin spectroscopy (μ SR) that detects signals of broken TRS. Phase-sensitive probes are crucial but still lacking. Here, we present signatures of chiral SC domains in CsV₃Sb₅ via phase-sensitive measurements.

CsV₃Sb₅ hosts a hexagonal structure, composed of alternating stacks of V₃Sb₅ slabs and Cs layers, among which vanadium ions form the Kagome net, seen in Fig. 1a. For the measurements, three devices (D1-D3) were fabricated by mechanically exfoliating nanoflakes from high-quality single crystals. The basic transport properties are presented in Extended Data Fig. 1.

Zero-field superconducting diode effect

The chiral SC was inspected by observing the SC diode effect (SDE), which depicts an asymmetry of the critical current (I_c) with respect to the direction of current flow in the absence of TRS and inversion symmetry (IRS)^{32,33}. TRS and IRS are disrupted either internally or externally. In the case of internal TRS breaking, magnetic

* Equal contributions

† zhiweiwang@bit.edu.cn

‡ wucongjun@westlake.edu.cn

§ linxiao@westlake.edu.cn

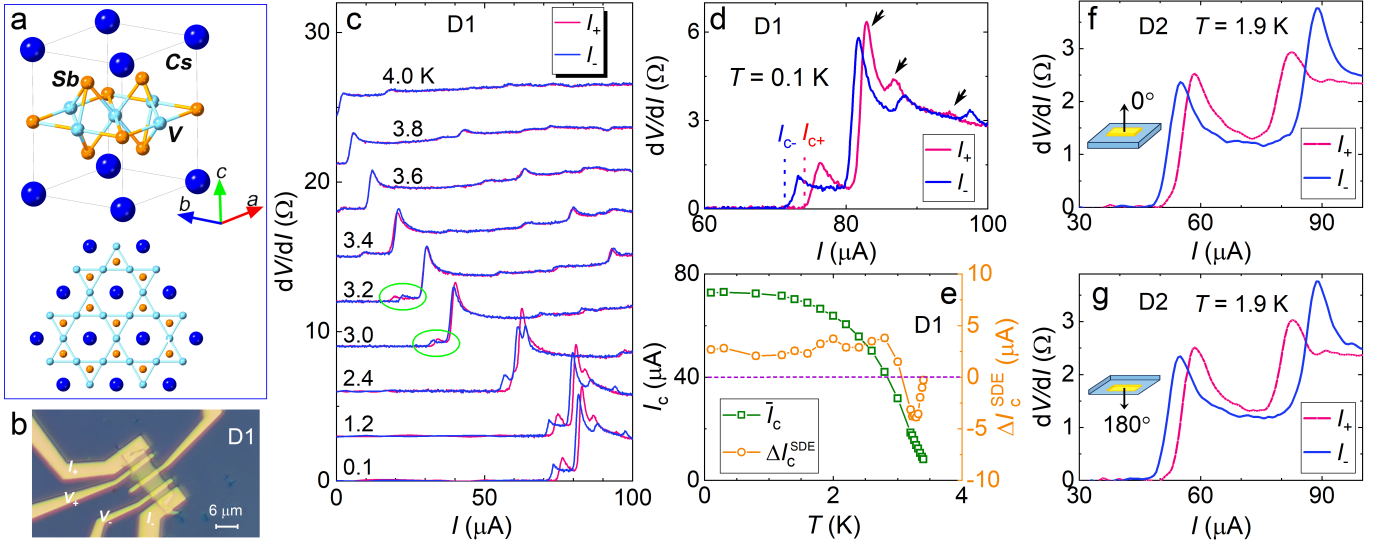


FIG. 1. **Zero-field superconducting diode.** **a**, Crystal structure of CsV_3Sb_5 . **b**, Optical image of the device D1. **c**, Differential resistance (dV/dI) as a function of d.c. current bias (I) at various T for D1. The red and blue curves are collected in positive (I_+) and negative (I_-) bias regimes, respectively. Curves are offset from each other by 3Ω for clarity. **d**, Enlarged curve of **c** at $T = 0.1 \text{ K}$. **e**, T -dependence of average critical current (\bar{I}_c) and ΔI_c^{SDE} , where $\bar{I}_c = (I_{c+} + I_{c-})/2$ and $\Delta I_c^{\text{SDE}} = I_{c+} - I_{c-}$. **f** and **g**, dV/dI versus I for D2 with the setup at 0° and 180° configurations, respectively.

field (B)-free SDEs^{34–36} are realized, in turn reflecting the nature of pairing symmetry³³. To examine intrinsic properties, non-SC contacts were made by gold deposition, seen in Fig. 1b. The cryostat was warmed up to room temperature (T) to fully release residual flux trapped in the SC magnet prior to experiments. In Supplementary Note 1, additional procedures were implemented to further eliminate any remaining field.

In Fig. 1c, the differential resistance (dV/dI) for D1 was measured by sweeping the d.c. current (I) at zero B and various T . I_c evolves with the reduction of T along with a noticeable inequivalence between the positive (I_+) and negative (I_-) bias regimes. A magnified curve at $T = 0.1 \text{ K}$ is specified in Fig. 1d, in which I_{c+} along the positive direction is larger than I_{c-} along the negative one ($\Delta I_c^{\text{SDE}} = I_{c+} - I_{c-} \approx 3 \mu\text{A}$), indicating non-reciprocity. Additionally, several non-reciprocal transition features (marked by arrows) are observed above I_c . Its relation to SC domain structures will be explained later. Fig. 1e displays the average \bar{I}_c and ΔI_c^{SDE} versus T . As T declines, ΔI_c^{SDE} shows a peculiar sign switching slightly below the SC transition temperature ($T_c \approx 3.5 \text{ K}$), as indicated by circles in Fig. 1c, and eventually its polarity becomes stable. This polarity variation is weird, distinct from what was reported^{33,35}. In Extended Data Fig. 2, the SDE polarity could be reversed after thermal cycling from T slightly above T_c , which also shows the magnitude alteration of \bar{I}_c and ΔI_c^{SDE} . Relevant data, including half-wave rectification, are shown in Extended Data Fig. 3, 4. It is noteworthy that the SDE signals remained unchanged even when the setup was reversed in Fig. 1f and g, underscoring the prominent role played by the spontaneous TRS-breaking, instead of from the environment.

See more discussion in Supplementary Note 1.

The presence of thermal switching and polarity variation in zero-field SDEs hints the existence of dynamic orders in an internal TRS-breaking background. A plausible candidate is chiral SC domains, which will be further elucidated below. This finding is hardly explained by the chiral charge order inherited from the normal state (see discussion in Methods).

Superconducting interference patterns

In Fig. 2a, b, we measured dV/dI at selective values of B for D1 and plotted its color map in the I - B plane. Intriguingly, three sets of periodic oscillation profiles (I_c , I'_c and I''_c) are resolved in Fig. 2a, traced by three transition peaks marked by dashed curves in Fig. 2b. Similar patterns with distinct periodicity for D2 are presented in Fig. 2c. More data are in Extended Data Fig. 5-7.

Such double-slit patterns vividly imitate the SC interference patterns (SIPs), which would be obtained from a Little-Parks (LP) device as depicted in Fig. 2d. In such a device, the magnetic flux threading in hollow regions modulates the loop supercurrent, as sketched in Fig. 2f³⁷. The fluxoid quantization within an enclosed area leads to the superfluid velocity $v_e = 2\pi\hbar/(m^*L_c)(n - \phi/\phi_0)$, where m^* is the Ginzburg-Landau (GL) effective mass; L_c is the loop circumference; n is the closest integer to ϕ/ϕ_0 with $\phi_0 = hc/(2e)$ the flux quantum and $\phi = BS_\phi$ the flux enclosed by the loop; S_ϕ is the field threading area. It subsequently leads to a modulation of the SC condensation wavefunction Ψ_e as $\Delta|\Psi_e|^2 \sim (n - \phi/\phi_0)^2$. Then, the variation of the GL critical current is yielded as (see more discussion in Supplementary Note 2):

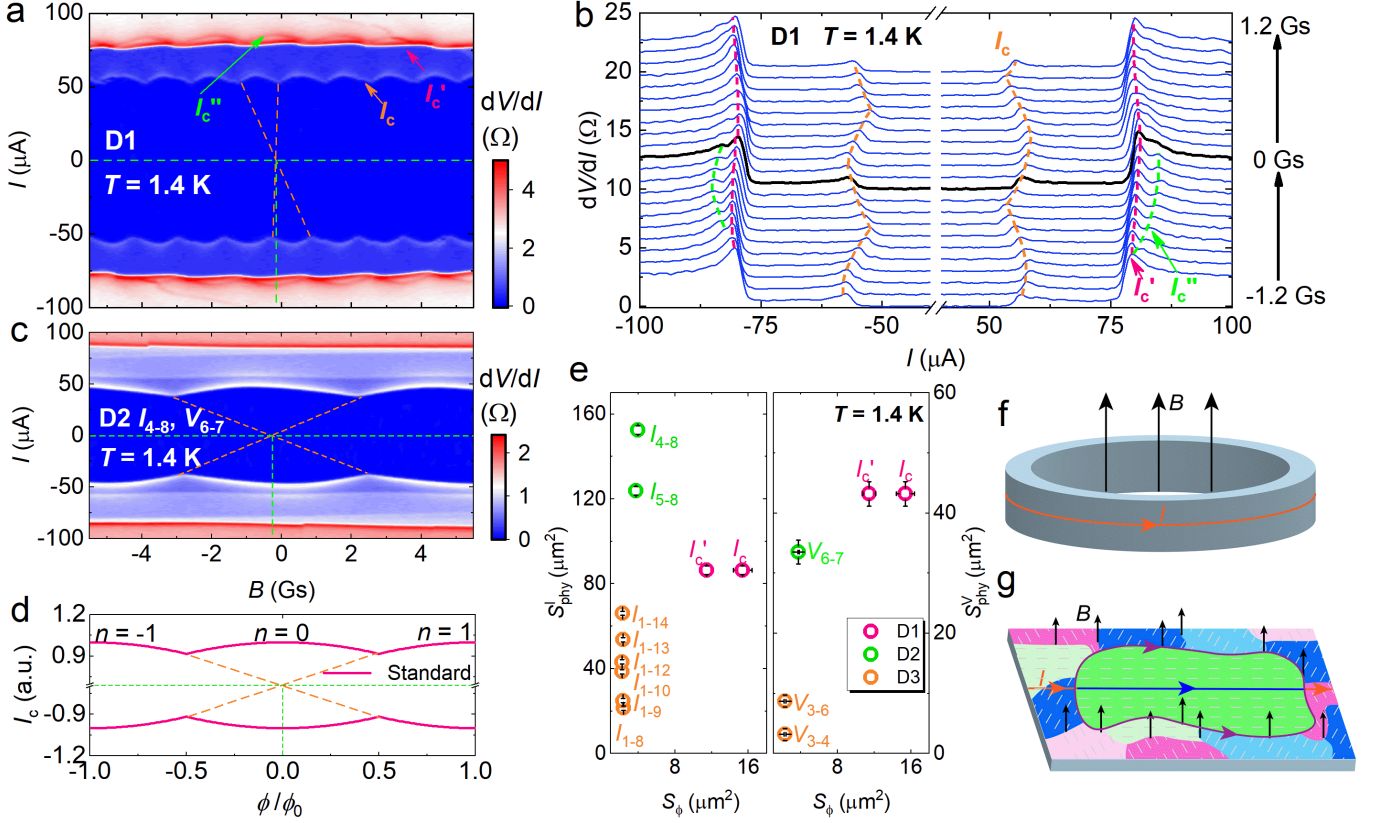


FIG. 2. **Superconducting interference patterns on intrinsic CsV₃Sb₅ flakes.** **a**, SIPs on D1 measured at 1.4 K. See the patterns at a broader scale in Extended Data Fig. 5. **b**, Corresponding sets of dV/dI versus I at $-1.2 < B < 1.2$ Gs. Three sets of SIPs in **a** are traced out by the transition anomalies, delineated by dashed curves and denoted as I_c , I'_c and I''_c . **c**, SIPs on D2 measured at 1.4 K. **d**, Standard SIP derived from Eq. 1. The orange dashed lines in **a**, **c** and **d** connect the minimum of the oscillation profiles within the $n = 0$ segment. Their intersection, offset from $B = 0$ Gs, reveals the deviation from the standard model. **e**, Physical area ($S_{\text{phy}}^{I/V}$) versus the flux penetration area (S_ϕ) for D1, D2 and D3. $S_{\text{phy}}^{I/V}$ is the area between a couple of current/voltage electrodes denoted by a numerical pair (see Fig. 1b and Extended Data Fig. 4, 5). The data was extracted from Fig. 2a, c and Extended Data Fig. 6, 7. The error bars indicate uncertainties in the determination of $S_{\text{phy}}^{I/V}$ and S_ϕ . S_ϕ is insensitive to the variation of current or voltage electrodes, e.g. for D3, implying that S_ϕ is related to a specific area between two certain terminals. In Extended Data Fig. 7, the primary SIP for V_{3-6} of D3 arises from regions between V_{3-4} , explaining the same S_ϕ for V_{3-6} and V_{3-4} in panel right. **f**, Illustration of the LP device. **g**, Sketch of domain network in CsV₃Sb₅ devices. The supercurrent passes through the domains both along the boundaries and within the bulk. The pink, blue and green regions represent three types of C_2 rotational SC domains. Each hosts two degenerate phases of opposite chirality, as denoted by the heavy and light colors. Please refer to details in Discussion.

$$\frac{\Delta I_c^{\text{SIP}}}{I_c} \sim -g \left(\frac{2\pi\xi}{L_c} \right)^2 \left(n - \frac{\phi}{\phi_0} \right)^2 \quad (1)$$

where ξ is the GL coherence length and g is a constant of order one.

It seems counterintuitive that such phenomena exist in unpatterned SC devices as in our case. A plausible explanation may lie in the existence of edge supercurrent (I_e) forming closed loop structures at certain boundaries³⁸. According to the oscillation period (ΔB_p) extracted from Fig. 2a, c and Extended Data Fig. 6, 7, S_ϕ is calculated through $S_\phi = \phi_0/\Delta B_p$ and is compared with $S_{\text{phy}}^{I/V}$, the physical area enclosed by the current/voltage electrodes, in Fig. 2e. Note that S_ϕ is detected by varying the cur-

rent (voltage) terminals, while keeping the voltage (current) terminals unchanged for a single device. S_ϕ is much smaller than S_{phy}^I and S_{phy}^V . No scaling relationships are observed among them. This finding suggests that I_e flows along a specific boundary within the sample³⁸, aligning with the expectation of chiral SC domains.

In a chiral SC, domain structures between opposite chiralities are often established due to spontaneous symmetry breaking³⁹. For CsV₃Sb₅, we will argue below that there is a network of domain walls guiding the flow of I_e (see details in Discussion). At the walls, SC order parameters are relatively suppressed compared to the bulk¹⁸. Thus, the magnetic flux passes through the walls and penetrates the domain on the scale of the Pearl length $\Lambda_p = 2\lambda^2/d$, where λ is the London length. Given

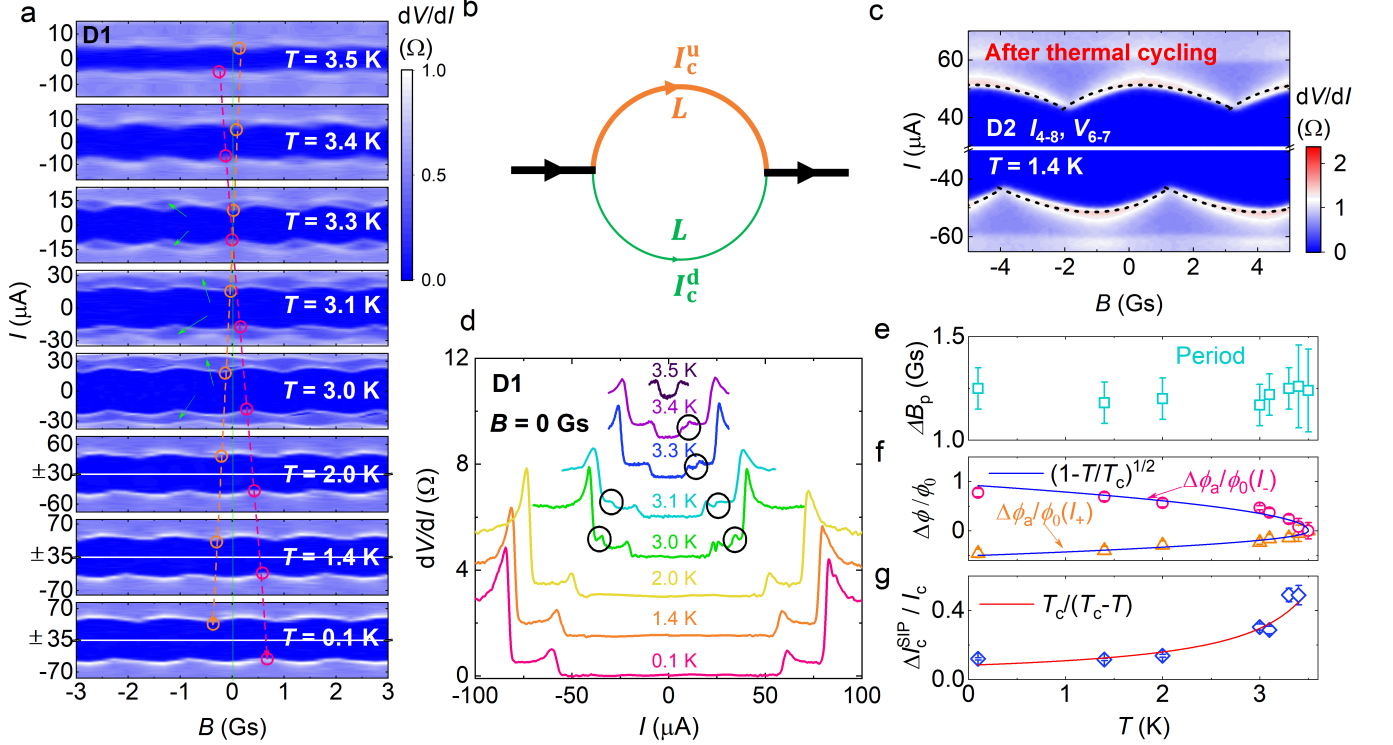


FIG. 3. **Temperature evolution of SIPs for D1.** **a**, SIPs on D1 measured at various T . Open circles, spotted at the nearest minima of I_c around 0 Gs, tracks the counter-shift of I_+ and I_- branches. A new SIP appears at $T > 3$ K marked by arrows. **b**, Illustration of domain inversion asymmetry. The critical current passing through the upper and lower branches are unequal: $I_c^u \neq I_c^d$. L is the inductance. **c**, Numerical simulation (dashed curves) of the observed SIPs in D2, incorporating domain inversion asymmetry. **d**, dV/dI versus I at $B = 0$ Gs. A sudden peak emerges at $T > 3$ K enclosed by circles, corresponding to the new SIP indicated in **a**. **e**, T -evolution of period (ΔB_p). **f**, Relative phase counter-shift versus T . $\Delta\phi_a(I_{\pm})$ is obtained by comparing $\phi_a(I_{\pm})(T)$ with respect to the value at 3.5 K. The solid curves are fits to $\sqrt{1 - T/T_c}$. **g**, T -dependence of normalized oscillation amplitude ($\Delta I_c^{\text{SIP}}/I_c$). The solid curve is a fit to the GL theory. The error bars indicate uncertainties in determination of extracted values.

$\lambda(0 \text{ K}) \approx 0.4 \mu\text{m}$ ³¹, one yields $\Lambda_p(0 \text{ K}) \approx 8 \mu\text{m}$ for D1 with the thickness $d \approx 40 \text{ nm}$, which is longer than the domain length scale ($\sqrt{S_{\phi}}$), indicating the penetration of flux throughout the domain. The edge supercurrent flows along the wall such that the domain enclosed by the supercurrent loop acts like a hollow (weak shielding of B) that serves as a basis for the LP effect, as illustrated in Fig. 2g. In Supplementary Note 3, we discuss that the circulating supercurrent occurring in the bulk does not induce oscillation patterns.

The preceding discussion primarily revolves around domain boundaries, by assuming a priori that the edge and bulk wave functions (Ψ_e and Ψ_b) are treated separately. Indeed, the applied current (I) passes through both the domain bulk (I_b) and edge. As I approaches to I_c , I is self-distributed such that both the boundary and bulk regions tend toward the normal state. We propose that the sharp double-slit SIPs stems from the contribution of I_e , and I_b gives rise to a slow, broad evolution of I_c , as shown in Extended Data Fig. 5b. In the figure, the double-slit SIP is enveloped by a broader Fraunhofer-like pattern, likely induced by a local Josephson junction between neighboring domains, displaying the superposition

of domain edge and bulk contributions. See more discussion in the Supplementary Note 4, 5 and Methods.

Note that I_c is not solely determined by the intrinsic critical current, but rather influenced by the connection strength between SC domains. The randomness in domain distribution and the spatial variation in the connection strength lead to the variation of I_c across different voltage terminals in Extended Data Fig. 4 as well as the multiple transition features in Fig. 1d. The dynamics of domains account for the I_c modulation after thermal cycling in Extended Data Fig. 2. In Extended Data Fig. 7, the sharp SIP exists only between terminals V_{3-4} , while others show obscure or even indiscernible patterns. This suggests specific domain structure requirements for observing SIPs, which, we consider, requires a SC domain of suitable dimensions (about $10 \mu\text{m}^2$) and regular geometries, preferably hosting a discrete I_c distinct from the surrounding region in series. Discussion about the possibility of other scenarios is presented in Methods.

Broken time-reversal and inversion symmetry

Upon close inspection of SIPs in Fig. 2a, c, we discern a slight shift of the pattern symmetry center, marked by

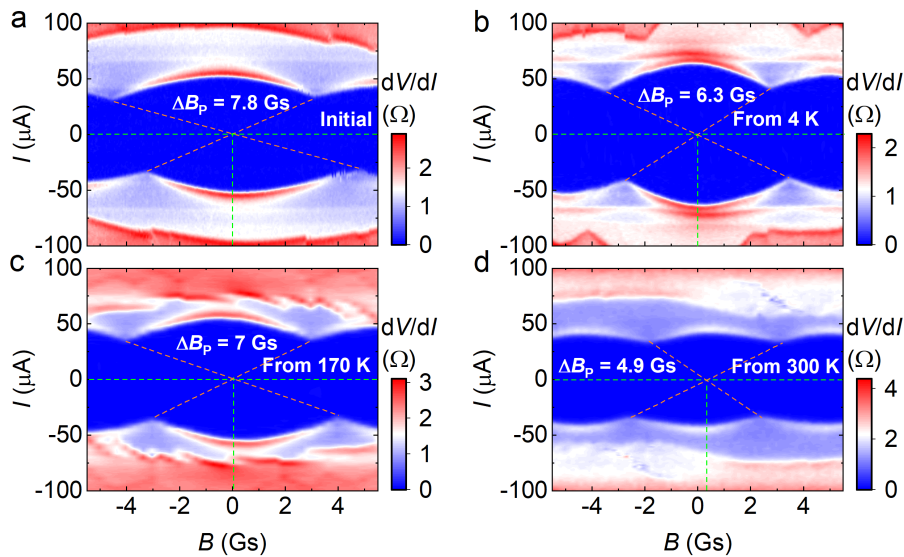


FIG. 4. **Thermal modulation of SIPs measured at 1.9 K for D2.** **a**, Initial SIPs. **b**, SIPs acquired from multiple thermal cycling from $T = 4$ K, slightly above T_c . **c**, SIPs obtained from multiple thermal cycling from $T = 170$ K, above T_{CDW} . **d**, SIPs obtained from multiple thermal cycling from $T = 300$ K. The dashed lines are guides to eyes.

the intersection of dashed lines, compared to the standard model in Fig. 2d. Its deviation from zero field, defined as B_{in} , signifies a broken TRS⁴⁰. In Supplementary Fig. 3, SIPs at 0° and 180° configurations show indiscernible phase differences with the positive flux direction fixed relative to the flipped sample, indicating the predominant role of internal B in determining the phase. In Supplementary Fig. 4, sweeping field within a range of $|B| < 6$ Gs does not induce vortex trapping. Therefore, B_{in} arises from an intrinsic TRS-breaking effect.

The measured B_{in} ranges from negligibly small to about 0.8 Gs in Supplementary Fig. 3a. The maximum is about threefold the internal magnetic field detected by μ SR in the charge order phase⁶, which is considered as a chiral flux phase composed of clockwise and anti-clockwise flux loops at the lattice sites in CsV_3Sb_5 ⁴¹. μ SR detects local field created by the imbalances of fluxes. The average B_{in} at the micron scale in the normal state is thought to be largely eliminated, as supported by recent magneto-Kerr experiments that detected negligible TRS-breaking signals⁴². Moreover, the thermal modulation of the phase is shown below. Therefore, B_{in} detected here stems, at least partially, from the SC order.

Upon further scrutiny of Fig. 2a,c and 3a, we find the periodic profile is asymmetric within each segment of I_{c+} and I_{c-} , i.e., lacking of a reflection symmetry. It also shows that $I_{c+}(B) \neq I_{c-}(B)$, indicating broken IRS⁴⁰. These features could be explained by asymmetry embedded in domain formation. As illustrated by the following model: The current loop is divided into two segments (up/down) with unequal critical current ($I_c^u \neq I_c^d$) in Fig. 3b due to the domain asymmetry. The additional flux ϕ_a appears from the self-inductance due to the imbalance between I_c^u and I_c^d .

Obviously, ϕ_a is odd with respect to the current direc-

tion. Adding ϕ_a to Eq. 1 produces an asymmetry in SIPs as shown by dashed lines in Fig. 3c that closely mimics the experimental results. More discussion of the asymmetric SIPs is presented in Supplementary Note 4. The presence of broken TRS and IRS in SIPs yields zero-field SDEs.

Let us now gain more insights into the SIPs by analyzing the T -evolution. First, a new SIP emerges near T_c , marked by arrows in Fig. 3a. It coincides with a sudden peak circled in the dV/dI curves in Fig. 3d, implying the formation of a new supercurrent loop. This highlights domain dynamics near T_c . Second, the period $\Delta B_p(T)$ is nearly constant within the experimental margin in Fig 3e, in contrast to the fact that $\Lambda_p(T)$ diverges as T approaches T_c . This supports our argument that S_ϕ is truncated by the size of domains. Third, the I_\pm branches of a SIP exhibit an increasingly pronounced counter-shift in phase as T lowers in Fig. 3a, accounting for the SDE evolution in Fig. 1e. In Fig. 3f, the counter-shift scales as $\phi_a(I_\pm) \sim \mp\sqrt{1 - T/T_c}$ as referred from Supplementary Note 4. Finally, combining Eq. 1 and the GL theory, one deduce the oscillation amplitude $\Delta I_c^{SIP}/I_c \sim \xi^2 \sim T_c/(T_c - T)$, which fits our results well in Fig. 3g.

Modulation of dynamic SC domains

The SC domain structure is closely linked with the distribution of local defects/strains and domain dynamics influenced by thermal histories. Accordingly, we observed the SIPs are not always identical after thermal cycling, but sometimes exhibit quantitative, or even qualitative, variations. Fig. 4 shows remarkable thermal modulation of the domain size. ΔB_p evolves from an initial value of 7.8 Gs to 6.3 Gs after recoiling the device from 4 K, slightly above T_c . Subsequent cooling from 170 K re-

turns ΔB_p to 7 Gs. Further cooling from 300 K significantly alters ΔB_p to 4.9 Gs. Moreover, the patterns beyond the primary profile are substantially altered after thermal cycling. Combining Fig. 4 and Supplementary Fig. 3, 5, we also observe thermal modulation of phase and domain asymmetry. All these provide remarkable indications of the existence of dynamic SC domains. In Fig. 4b, ΔB_p shows noticeable changes although the thermal cycling is well below the charge ordering temperature ($T_{CDW} \approx 80$ K). Hence, the influence of charge order on the distribution of SC domains is not obvious. Moreover, the field modulation of SIPs is presented in Extended Data Fig. 8 and 9. They show either enhanced $|I_c|$ or “advanced” nature of hysteresis during field sweeps after field cooling, which is likely related to the rearrangement of SC domain walls driven by external B^{43} .

Discussion

The cumulative evidence from SDEs and SIPs supports the existence of a TRS breaking SC order in CsV_3Sb_5 . Nevertheless, the specific nature of its pairing state remains an open question. As discussed in Supplementary Note 6, previous theoretical studies have proposed a chiral $d_{x^2-y^2} \pm id_{xy}$ pairing symmetry characterized by a full SC gap^{28–30}, which could reconcile our results with the majority of prior experimental outcomes^{23–27}. However, the double-degenerate orders in a $d \pm id$ SC are insufficient to form a network of chiral domains.

In the normal state of CsV_3Sb_5 , the nematicity already disrupts the C_6 rotation symmetry of the electronic structure, transforming it into C_2 ¹⁹. There is possibility that SC developed from this state inherently possesses a nematic ground state. In this case, three types of C_2 SC domains, each accommodating two degenerate phases of opposite chirality, constitute sixfold domains, potentially responsible for the network configuration illustrated in Fig. 2g. The supercurrents flowing along domain boundaries lead to the observation of dynamic SIPs. Further details are given in Supplementary Note 7.

The method employed in this study may offer a simple probe for detecting domain edge supercurrents, contributing to the exploration of chiral SCs. The micro-sized SC domains could be further examined by high-resolution scanning probes capable of imaging current distributions. In the end, we note other scenarios, including pair-density-wave phase¹¹, chiral charge order⁶ or significant inhomogeneity, may explain certain aspects of our findings. Their possibilities are evaluated by extended discussion in Methods. A complete understanding of all these issues still requires further efforts.

Online content

Supplementary materials are available at the online version of the paper.

-
- [1] Balents, L. Spin liquids in frustrated magnets. *Nature* **464**, 199–208 (2010).
 - [2] Ko, W.-H., Lee, P. A. & Wen, X.-G. Doped kagome system as exotic superconductor. *Phys. Rev. B* **79**, 214502 (2009).
 - [3] Zhao, H. *et al.* Cascade of correlated electron states in the kagome superconductor CsV_3Sb_5 . *Nature* **599**, 216–221 (2021).
 - [4] Li, H. *et al.* Observation of unconventional charge density wave without acoustic phonon anomaly in kagome superconductors AV_3Sb_5 ($A=\text{Rb}, \text{Cs}$). *Phys. Rev. X* **11**, 031050 (2021).
 - [5] Ortiz, B. R. *et al.* Fermi surface mapping and the nature of charge-density-wave order in the kagome superconductor CsV_3Sb_5 . *Phys. Rev. X* **11**, 041030 (2021).
 - [6] Mielke III, C. *et al.* Time-reversal symmetry-breaking charge order in a kagome superconductor. *Nature* **602**, 245–250 (2022).
 - [7] Jiang, Y.-X. *et al.* Unconventional chiral charge order in kagome superconductor KV_3Sb_5 . *Nat. Mater.* **20**, 1353–1357 (2021).
 - [8] Guo, C. *et al.* Switchable chiral transport in charge-ordered kagome metal CsV_3Sb_5 . *Nature* **611**, 461–466 (2022).
 - [9] Nie, L. *et al.* Charge-density-wave-driven electronic nematicity in a kagome superconductor. *Nature* **604**, 59–64 (2022).
 - [10] Li, H. *et al.* Rotation symmetry breaking in the normal state of a kagome superconductor KV_3Sb_5 . *Nat. Phys.* **18**, 265–270 (2022).
 - [11] Chen, H. *et al.* Roton pair density wave in a strong-coupling kagome superconductor. *Nature* **599**, 222–228 (2021).
 - [12] Ortiz, B. R. *et al.* CsV_3Sb_5 : A Z_2 topological kagome metal with a superconducting ground state. *Phys. Rev. Lett.* **125**, 247002 (2020).
 - [13] Ivanov, D. A. Non-Abelian statistics of half-quantum vortices in p -wave superconductors. *Phys. Rev. Lett.* **86**, 268–271 (2001).
 - [14] Leggett, A. J. A theoretical description of the new phases of liquid ^3He . *Rev. Mod. Phys.* **47**, 331–414 (1975).
 - [15] Kallin, C. & Berlinsky, J. Chiral superconductors. *Rep. Prog. Phys.* **79**, 054502 (2016).
 - [16] Schemm, E., Gannon, W., Wishne, C., Halperin, W. & Kapitulnik, A. Observation of broken time-reversal symmetry in the heavy-fermion superconductor UPt_3 . *Science* **345**, 190–193 (2014).
 - [17] Jiao, L. *et al.* Chiral superconductivity in heavy-fermion metal UTe_2 . *Nature* **579**, 523–527 (2020).
 - [18] Ming, F. *et al.* Evidence for chiral superconductivity on a silicon surface. *Nat. Phys.* **19**, 500–506 (2023).
 - [19] Li, H. *et al.* Unidirectional coherent quasiparticles in the high-temperature rotational symmetry broken phase of AV_3Sb_5 kagome superconductors. *Nat. Phys.* **19**, 637–642 (2023).
 - [20] Zheng, L. *et al.* Emergent charge order in pressurized kagome superconductor CsV_3Sb_5 . *Nature* **611**, 682–687 (2022).

- [21] Zhao, C. *et al.* Nodal superconductivity and superconducting domes in the topological kagome metal CsV₃Sb₅. Preprint at <https://arxiv.org/abs/2102.08356> (2021).
- [22] Guguchia, Z. *et al.* Tunable unconventional kagome superconductivity in charge ordered RbV₃Sb₅ and KV₃Sb₅. *Nat. Commun.* **14**, 153 (2023).
- [23] Mu, C. *et al.* S-wave superconductivity in kagome metal CsV₃Sb₅ revealed by ^{121/123}Sb NQR and ⁵¹V NMR measurements. *Chin. Phys. Lett.* **38**, 077402 (2021).
- [24] Duan, W. *et al.* Nodeless superconductivity in the kagome metal CsV₃Sb₅. *Sci. China Phys. Mechan. Astron.* **64**, 107462 (2021).
- [25] Roppongi, M. *et al.* Bulk evidence of anisotropic s-wave pairing with no sign change in the kagome superconductor CsV₃Sb₅. *Nat. Commun.* **14**, 667 (2023).
- [26] Zhong, Y. *et al.* Nodeless electron pairing in CsV₃Sb₅-derived kagome superconductors. *Nature* **617**, 488–492 (2023).
- [27] Xu, H.-S. *et al.* Multiband superconductivity with sign-preserving order parameter in kagome superconductor CsV₃Sb₅. *Phys. Rev. Lett.* **127**, 187004 (2021).
- [28] Yu, S.-L. & Li, J.-X. Chiral superconducting phase and chiral spin-density-wave phase in a Hubbard model on the kagome lattice. *Phys. Rev. B* **85**, 144402 (2012).
- [29] Wu, X. *et al.* Nature of unconventional pairing in the kagome superconductors AV₃Sb₅ (A= K, Rb, Cs). *Phys. Rev. Lett.* **127**, 177001 (2021).
- [30] Rømer, A. T., Bhattacharyya, S., Valentí, R., Christensen, M. H. & Andersen, B. M. Superconductivity from repulsive interactions on the kagome lattice. *Phys. Rev. B* **106**, 174514 (2022).
- [31] Gupta, R. *et al.* Two types of charge order with distinct interplay with superconductivity in the kagome material CsV₃Sb₅. *Commun. Phys.* **5**, 232 (2022).
- [32] Ando, F. *et al.* Observation of superconducting diode effect. *Nature* **584**, 373–376 (2020).
- [33] Nadeem, M., Fuhrer, M. S. & Wang, X. The superconducting diode effect. *Nat. Rev. Phys.* **5**, 558–577 (2023).
- [34] Wu, H. *et al.* The field-free Josephson diode in a van der Waals heterostructure. *Nature* **604**, 653–656 (2022).
- [35] Jeon, K.-R. *et al.* Zero-field polarity-reversible Josephson supercurrent diodes enabled by a proximity-magnetized Pt barrier. *Nat. Mater.* **21**, 1008–1013 (2022).
- [36] Lin, J.-X. *et al.* Zero-field superconducting diode effect in small-twist-angle trilayer graphene. *Nat. Phys.* **18**, 1221–1227 (2022).
- [37] Barone, A. & Paterno, G. *Physics and applications of the Josephson effect*, vol. 1 (Wiley Online Library, 1982).
- [38] Wang, W. *et al.* Evidence for an edge supercurrent in the Weyl superconductor MoTe₂. *Science* **368**, 534–537 (2020).
- [39] Sigrist, M. & Ueda, K. Phenomenological theory of unconventional superconductivity. *Rev. Mod. Phys.* **63**, 239–311 (1991).
- [40] Wang, D., Wang, Q.-H. & Wu, C. Symmetry constraints on direct-current Josephson diodes. Preprint at <https://arxiv.org/abs/2209.12646> (2022).
- [41] Feng, X., Jiang, K., Wang, Z. & Hu, J. Chiral flux phase in the kagome superconductor AV₃Sb₅. *Sci. Bull.* **66**, 1384–1388 (2021).
- [42] Farhang, C., Wang, J., Ortiz, B. R., Wilson, S. D. & Xia, J. Unconventional specular optical rotation in the charge ordered state of kagome metal CsV₃Sb₅. *Nat. Commun.* **14**, 5326 (2023).
- [43] Kidwingira, F., Strand, J., Van Harlingen, D. & Maeno, Y. Dynamical superconducting order parameter domains in Sr₂RuO₄. *Science* **314**, 1267–1271 (2006).

Methods

Growth of single crystals

Single crystals of CsV_3Sb_5 were grown through flux methods by using Cs (purity 99.8%) bulk, V (purity 99.999%) pieces and Sb (purity 99.9999%) shot as the precursors and $\text{Cs}_{0.4}\text{Sb}_{0.6}$ as the flux agent. The starting elements were placed in an alumina crucible and sealed in a quartz ampoule in an argon-filled glove box. The ampoule was then gradually heated up to 1000 °C in 200 h and held at that temperature for 24 h in an oven. It was subsequently cooled down to 200 °C at a rate of 3.5 °C/h. The resulting product was immersed in deionized water to remove the flux. Finally, shiny CsV_3Sb_5 crystals with hexagonal shape were obtained.

Fabrication of devices

CsV_3Sb_5 nanoflakes were mechanically exfoliated from the bulk crystals using Nitto blue tape and transferred onto silicon substrates (5 mm × 5 mm) capped with 300 nm SiO_2 . The flakes were initially spin-coated with poly-methyl methacrylate (PMMA). Contacts were patterned by utilizing standard electron beam lithography (EBL) techniques (TESCAN VEGA LMS). After EBL patterning, the PMMA was immersed in a solution of methyl isobutyl ketone (MIBK)-isopropyl alcohol (IPA)(1:3) for 60 seconds, followed by rinsing with IPA. To improve the contact, the flakes were cleaned by Ar plasma, prior to deposition. Finally, the contacts with a width of 500 nm-1 μm were deposited with Ti (5 nm)/Au (80 nm) via electron beam evaporation.

Resistance measurements

The temperature dependence of resistance (R - T) for bulk and D1 from 1.8 K to 300 K was measured by standard four-terminal methods in Quantum Design physical property measurement system (PPMS). Other R - T curves measured around T_c were collected in an Oxford dilution refrigerator (Triton-500).

Measurements of superconducting diode effect

The zero-field superconducting diode effect was measured in Oxford dilution system (Triton-500) and Quantum Design Physical Property Measurement System (PPMS). Each measuring channel in Triton-500 was connected with a filter (QFilter-IIQdevil), positioned at the plate of mixing chamber and to a sample-protected measurement box, located at room temperature. Prior to measurements, the flux trapped in the superconducting magnet was completely released by warming the cryostat up to room temperature. Further procedures to eliminate the environmental field is presented in Supplementary Note 1. The differential resistance (dV/dI) in the I_+ and I_- regions was measured by sweeping the d.c. current bias (I) from 0 to $I_{\text{max}+}$ or $I_{\text{max}-}$. The current bias was supplied by a current source meter (Keithley 2450). A lock-in amplifier (Stanford Research, SR830) combined with a 1 or 10 M Ω buffer resistor was used to offer a small ac excitation current I_{ac} (11 – 173 Hz, 0.1 μA – 5 μA) to detect the differential resistance ($dV/dI = V_{\text{ac}}/I_{\text{ac}}$). The measurements were performed by standard four-terminal methods.

For the thermal cycling measurements, two methods were employed. The first method involved heating the sample

slightly above T_c by cryostat heater and subsequently re-cooling it to the target temperature. This process is slow, usually taking more than one hour. The second method utilized a 2 k Ω resistor, which was adhered on the SiO_2/Si substrate by silver paste as a heater. The local temperature of the device was then modulated via triggering the heater with pulsed (several seconds) milliampere current applied by a current source (Keithley 6221). This process was considerably faster, taking only a few minutes.

Measurements of interference patterns

The superconducting interference patterns (SIPs) were obtained by measuring dV/dI - I curves at various fixed magnetic field (B) with an interval of 0.1 Gs or 0.2 Gs per trace. A current source meter (Keithley 2440 or 2400) served as the power supply for the superconducting magnet in order to achieve precise control of B at sub-Gs levels. B is applied along c -axis, normal to the large plane of the flakes. During the measurements, the SIPs were detected within a narrow field range (e.g. -6 Gs to 6 Gs) after zero-field SDE measurements to prevent any influence from trapped vortices in samples or in the magnet, as referring to Supplementary Fig. 4. Subsequently, a higher B was applied to measure the broad pattern. We observed that magnetic vortices enter into the flakes and smear the SIPs when B exceeded 10 Gs, as depicted in Extended Data Fig. 5. The temperature evolution of the SIPs in Fig. 3a was detected after applying the high field. Note that 1 mA current corresponds to B of 1.2 Gs in Triton-500 and 1.6 Gs in PPMS, respectively. The measurements were performed by standard four-terminal methods.

Possibility of other interpretations

Before the detailed discussion, we summarize four key pieces of information from our findings:

1. Zero-field SDEs
2. Multiple transition peaks in dV/dI curves
3. Well-defined double-slit SIPs
4. All the features above modulated by thermal cycling from T slightly above T_c .

To account for all of these findings, we have proposed the existence of domain network of chiral SC orders in Discussion and Supplementary Note 7. In the following, we will extend discussion about the possibility of other scenarios.

Pair density wave The pair-density-wave (PDW) phase, as revealed by scanning tunneling microscopy (STM)¹¹, has been theoretically proposed to be chiral⁴⁴. The potential network formed by the chiral PDW domains may account for our findings. To distinguish this possibility from chiral SC order, further investigations invoking doped or pressurized Kagome superconductors with the suppression of intricate electronic orders^{20,26} are recommended.

Significant sample inhomogeneity The bulk CsV_3Sb_5 single crystal is of ultra-high quality and unlikely to be inhomogeneous, as indicated in Extended Data Fig. 1. Speculation about inhomogeneity generated during device fabrication processes is reasonable. While we cannot exclude the possibility that these processes

introduce some disorders, it seems unlikely that they cause significant inhomogeneity in our thick (40 nm) and highly crystalline exfoliated films. If such inhomogeneity is present, it is most likely due to sample degradation during the processes, which must be detrimental to the SC order. In contrast, T_c is increased by about 20% in our devices, similar to the previous report⁴⁵. Ref. 45 reported a systematic evolution of T_{cdw} with counter-evolution of T_c as the device thickness reduces. This phenomenon cannot be reconciled with the generation of significant inhomogeneity.

However, if substantial inhomogeneity exists in the device, it will result in discrete islands of SC order with varying I_c connected by weak links. In this case, the SC islands are asymmetric and in series, this could lead to zero-field SDE and multiple transition peaks given that TRS is broken, e.g. from the chiral charge order. The supercurrent across weak links may also induce Fraunhofer-like SIPs. But this is difficult to reconcile with the observation of the sharp double-slit SIPs. Additionally, such inhomogeneity is usually static, which fails to explain the thermal modulation near T_c .

Chiral charge order The chiral charge order ($T_{cdw} \approx 80$ K) breaks TRS in the normal state. Combined with the IRS breaking, e.g. geometric asymmetry, it potentially gives rise to zero-field SDEs, but it hardly accounts for the other three items. Subsequent concern involves the possible existence of chiral charge order domains with normal state edge currents. Their fate in the SC state is still unknown. Assuming that it persists into the SC state with the domain boundaries remaining normal, these boundaries could act as weak links cutting a homogeneous SC phase into pieces. The asymmetry of the domain and spatial variation in link strength may contribute to zero-field SDEs and multiple transition peaks. The supercurrent across weak links may induce Fraunhofer-like SIPs, however this is challenging to account for the distinct double-slit SIPs in the absence of edge supercurrent. Additionally, the charge order is usually static near T_c , which fails to explain the dynamic properties. In short, the charge order domain scenario could potentially account for terms 1 and 2 under substantial assumptions, it faces challenges in elucidating terms 3 and 4.

Composite domain network The scenarios discussed above struggle to explain the crucial information of our results (terms 3 and 4). The distinct features of the sharp double-slit SIPs are usually associated with closed edge supercurrents and their dynamic properties are highly correlated with the SC transition. An intuitive explanation for these phenomena lies in the emergence of chiral SC domains. We have explained that a two-component chiral SC order parameter (e.g. $d \pm id$) alone is insufficient to generate a domain network, the formation of which requires the additional presence of rotation symmetry breaking from C_6 to C_2 symmetry in CsV_3Sb_5 . Below, we propose an alternative scenario involving a composite domain network, where the two-component SC domains emerge on top of multiple SC regions already separated by weak links from, for instance, significant inhomogeneity. Though the likelihood of this scenario is minimal, it could potentially offer an additional explanation for our

observations.

Data availability

Data are available from the corresponding author upon reasonable request.

- [44] Zhou, S. & Wang, Z. Chern Fermi pocket, topological pair density wave, and charge-4e and charge-6e superconductivity in kagomé superconductors. *Nat. Commun.* **13**, 7288 (2022).
- [45] Song, B. *et al.* Anomalous enhancement of charge density wave in kagome superconductor CsV_3Sb_5 approaching the 2D limit. *Nat. Commun.* **14**, 2492 (2023).
- [46] Liang, Z. *et al.* Three-dimensional charge density wave and surface-dependent vortex-core states in a kagome superconductor CsV_3Sb_5 . *Phys. Rev. X* **11**, 031026 (2021).
- [47] Fu, Y. *et al.* Quantum transport evidence of topological band structures of kagome superconductor CsV_3Sb_5 . *Phys. Rev. Lett.* **127**, 207002 (2021).

Acknowledgments The authors are grateful to Lin Jiao and Chunyu Guo for the helpful discussion. This research is supported by Zhejiang Provincial Natural Science Foundation of China for Distinguished Young Scholars under Grant No. LR23A040001. C.W. is supported by the National Natural Science Foundation of China under the Grants No. 12234016 and No. 12174317. T.L. acknowledges support from the China Postdoctoral Science Foundation (Grant No. 2022M722845 and No. 2023T160586). This work has been supported by the New Cornerstone Science Foundation. X.L. acknowledges the support by the Research Center for Industries of the Future (RCIF) at Westlake University under Award No. WU2023C009. The authors thank the support provided by Dr. Chao Zhang from Instrumentation and Service Center for Physical Sciences at Westlake University.

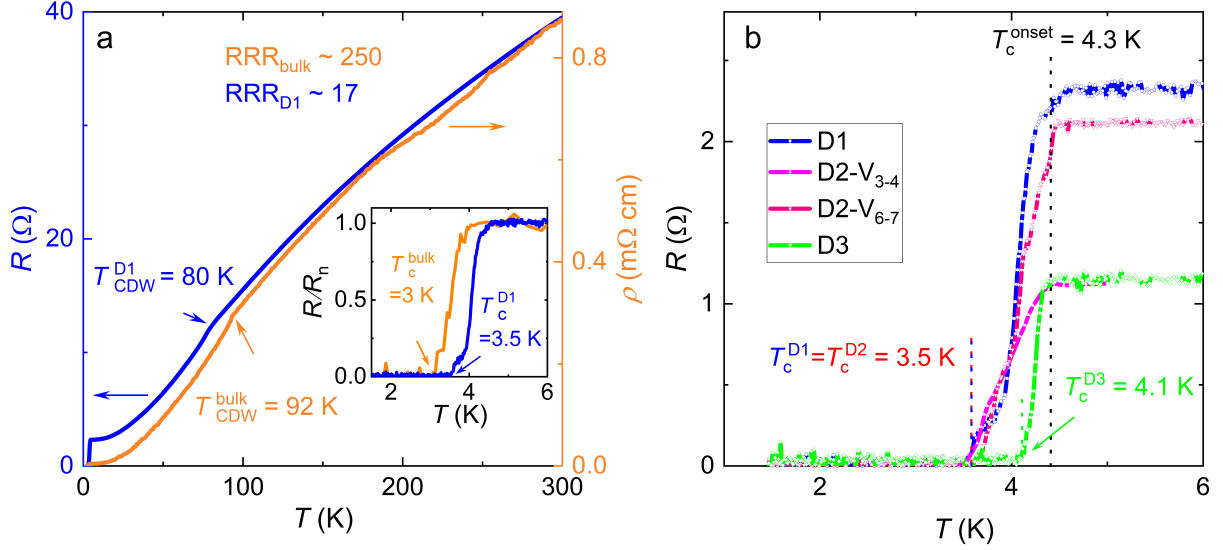
Author contributions T.L. fabricated the devices and did the transport measurements assisted by Z.X., J.W., Z.L. and X.Y.. J.L. prepared the samples supervised by Z.W. and Y.Y.. Z.P. did theoretical calculations supervised by C.W.. T.L., Z.P. and X.L. prepared the figures. X.L. wrote the paper with the inputs from T.L., Z.P. and C.W.. X.L. led the project. All authors contributed to the discussion.

Competing interests The authors declare no competing interests.

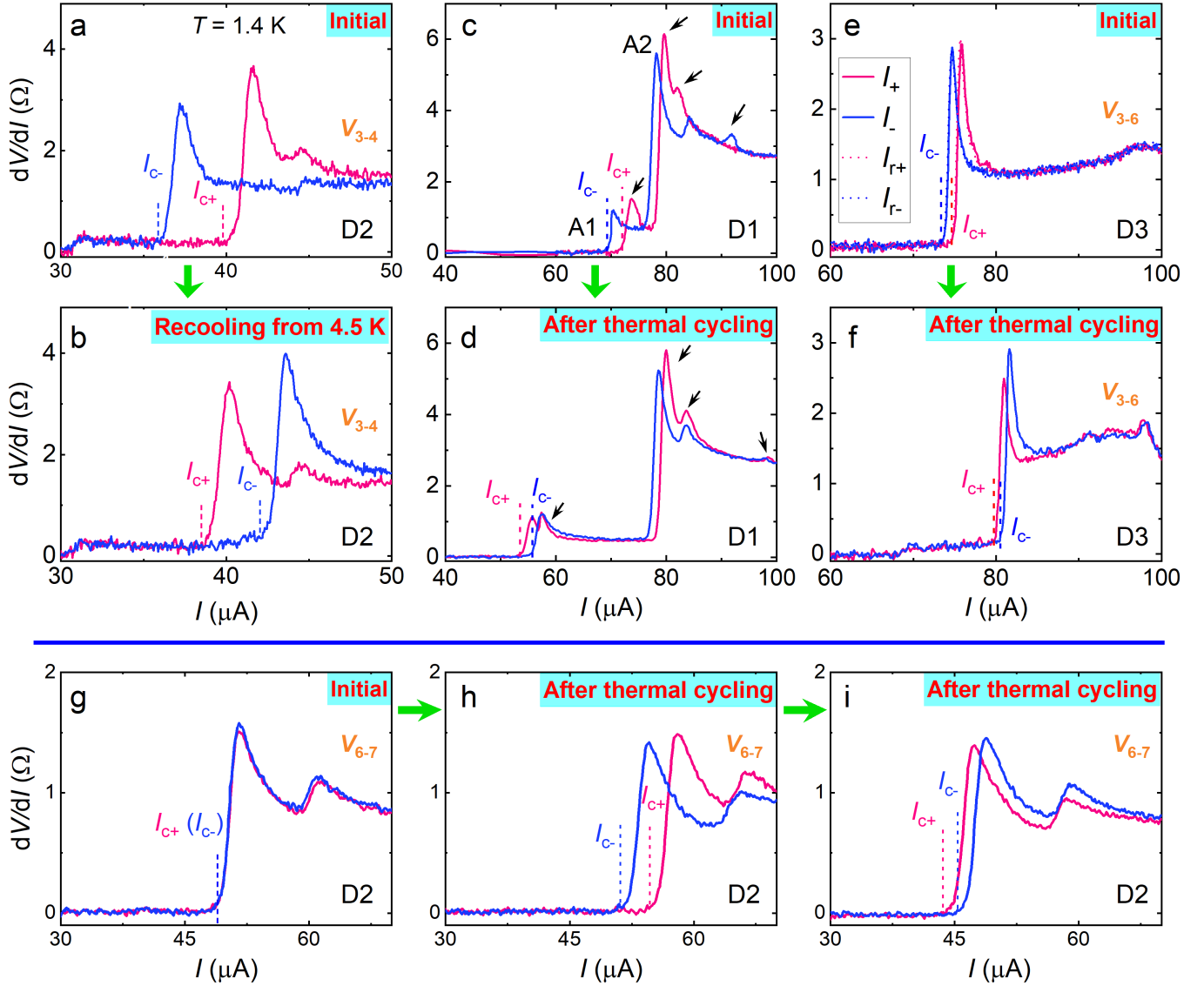
Additional information

Supplementary information are available at the online version of the paper.

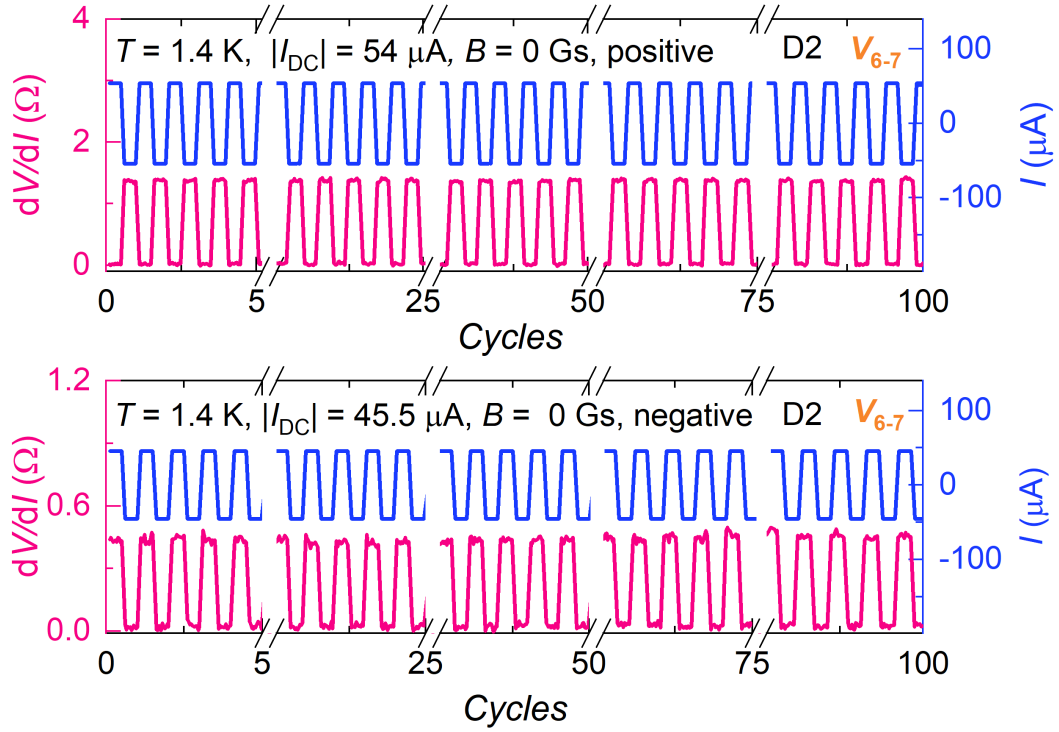
Correspondence and requests for materials should be addressed to Zhiwei Wang, Congjun Wu or Xiao Lin.



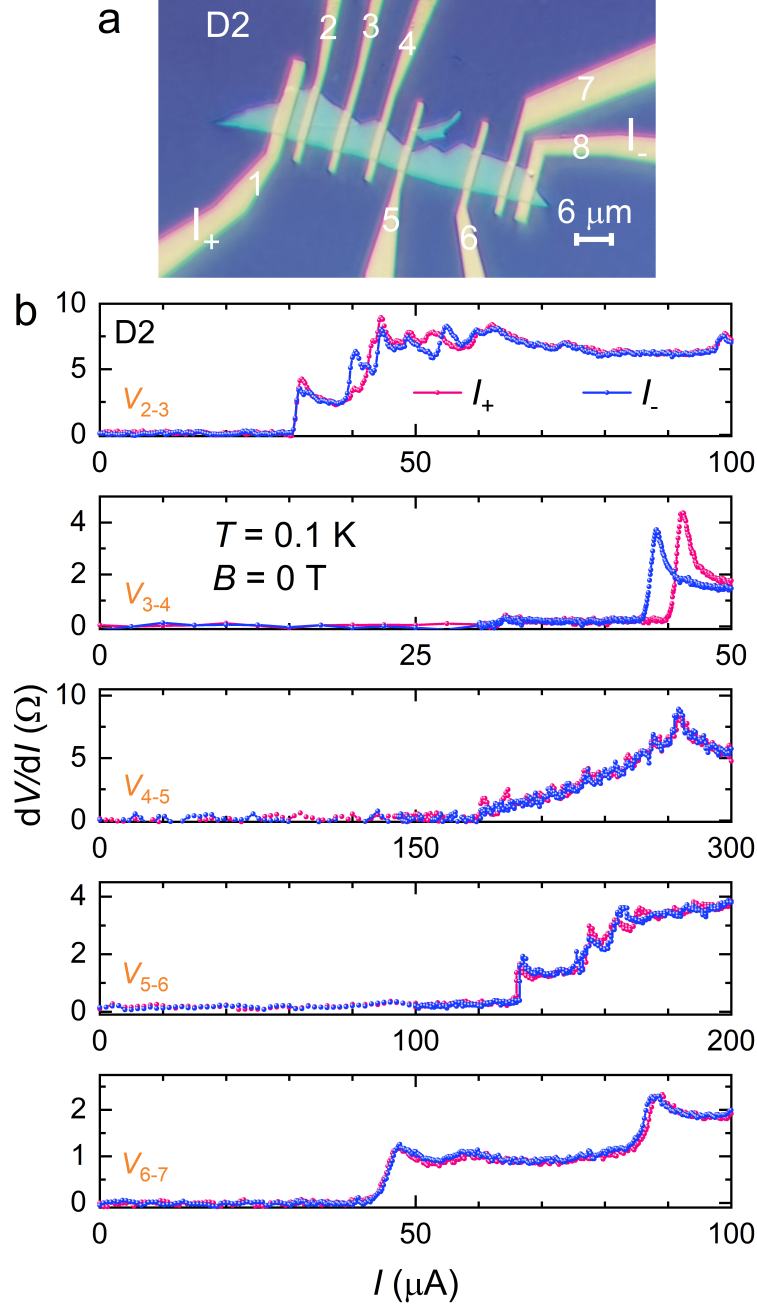
Extended Data Fig. 1. **Temperature dependence of resistance for D1-D3.** **a**, T -dependence of ρ for the bulk single crystal (B1) and R for a mechanically exfoliated specimen (D1) in the full- T range. The residual-resistance-ratio (RRR) amounts to 250 in B1, among the highest value of the literature^{5,12,46,47}, highlighting the ultra-high quality of our crystals. The transition to chiral charge density wave (CDW) phase in B1 appears at $T_{CDW} \approx 92$ K¹², accompanied by a SC phase transition at $T_c \approx 3$ K (determined at zero-resistance), consistent with previous reports¹². In D1, T_{CDW} is reduced to 80 K with the enhancement of T_c to 3.5 K, as reported in the literature⁴⁵. The inset presents the normalized resistance R/R_n around T_c , where R_n is the normal state resistance. **b**, T -dependence of R around T_c for D1-D3. For D2, we present the data collected at two sets of terminals: V_{3-4} and V_{6-7} . The onset temperature of the superconducting transition (T_c^{onset}) for D1-D3 is similar, about 4.3 K. T_c for D3 amounts to 4.1 K, which is higher than that of D1 and D2 (about 3.5 K). Note that T_c of D2 measured at V_{3-4} and V_{6-7} is slightly different, reflecting different domain characteristics in-between the terminals. The thickness (d) of D1-D3 is about 40 nm.



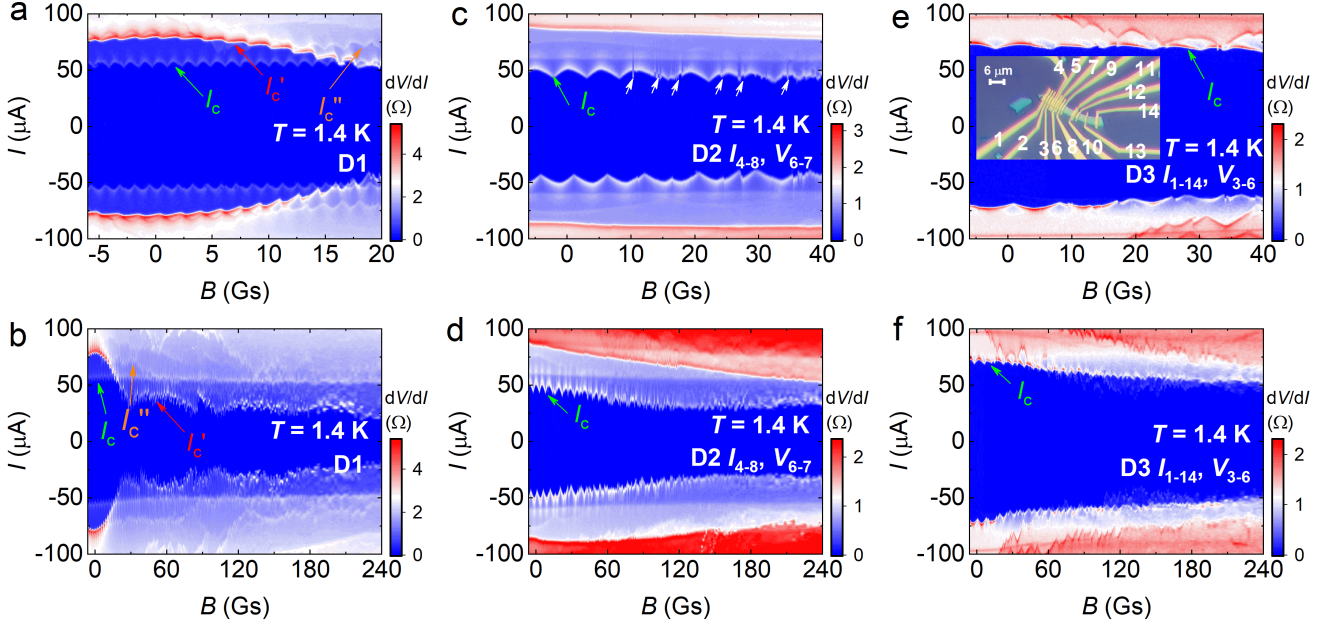
Extended Data Fig. 2. **Thermal modulation of zero field SDE for D1-D3 measured at $T = 1.4$ K.** **a-b**, dV/dI versus I for terminals V_{3-4} of D2 before (a) and after recoiling from 4.5 K, slightly above T_c (b). **c-d**, dV/dI versus I for D1 before (c) and after thermal cycling (d). **e-f**, dV/dI versus I for terminal V_{3-6} of D3 before (e) and after thermal cycling (f). In e, the measurement includes four branches: sweeping I from zero to positive (I_+), from positive back to zero (I_{r+}), from zero to negative (I_-) and from negative back to zero (I_{r-}). The hysteresis between I_+ (I_-) and I_{r+} (I_{r-}) is negligible, indicating the absence of thermal heating or current re-trapping effect. Below, several observations are made: 1. All the devices exhibit remarkable non-reciprocity. 2. Not only the polarity, but also the magnitude of ΔI_c^{SDE} and \bar{I}_c could be changed by thermal cycling. 3. The curves in c and d show multiple transition-like features with non-reciprocity (marked by arrows), probably related to the difference in I_c across different superconducting domain boundaries. 4. In c and d, the SDE polarity at A1 is reversed after thermal cycling, while the polarity at A2 remains unchanged. As discussed in Methods, the dynamic nature of SDEs with multiple transition peaks is unlikely to be fully explained by scenarios involving the combination of chiral charge order and certain sources of IR breaking such as geometric asymmetry and significant sample inhomogeneity. While, all of these could be reconciled with the existence of dynamic SC domains with broken TRS. Characteristics of the domains, such as domain asymmetry and inter-domain interaction, are randomly altered by thermal cycling (i.e. recoiling the system from above T_c). **g-i** dV/dI versus I for terminals V_{6-7} of D2 before (g) and after thermal cycling (h,i). V_{6-7} shows negligible non-reciprocity in the initial state. After thermal cycling, a finite SDE with either positive and negative polarity is induced.



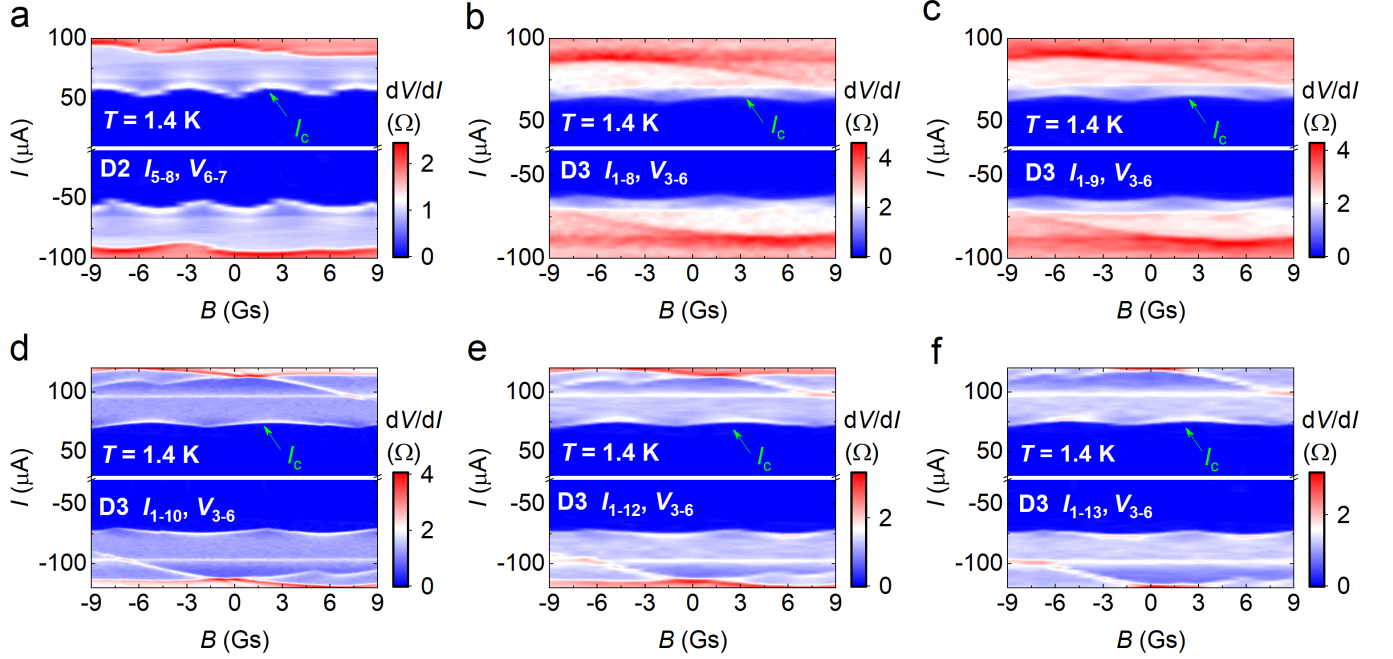
Extended Data Fig. 3. **Demonstration of half-wave rectification.** Direction-selective supercurrent transmission is demonstrated at V_{6-7} of D2 with positive (upper panel) and negative polarity (lower panel). The measurements were performed by alternating the current polarity every 15.5 seconds. SDE remains stable after 100 cycles.



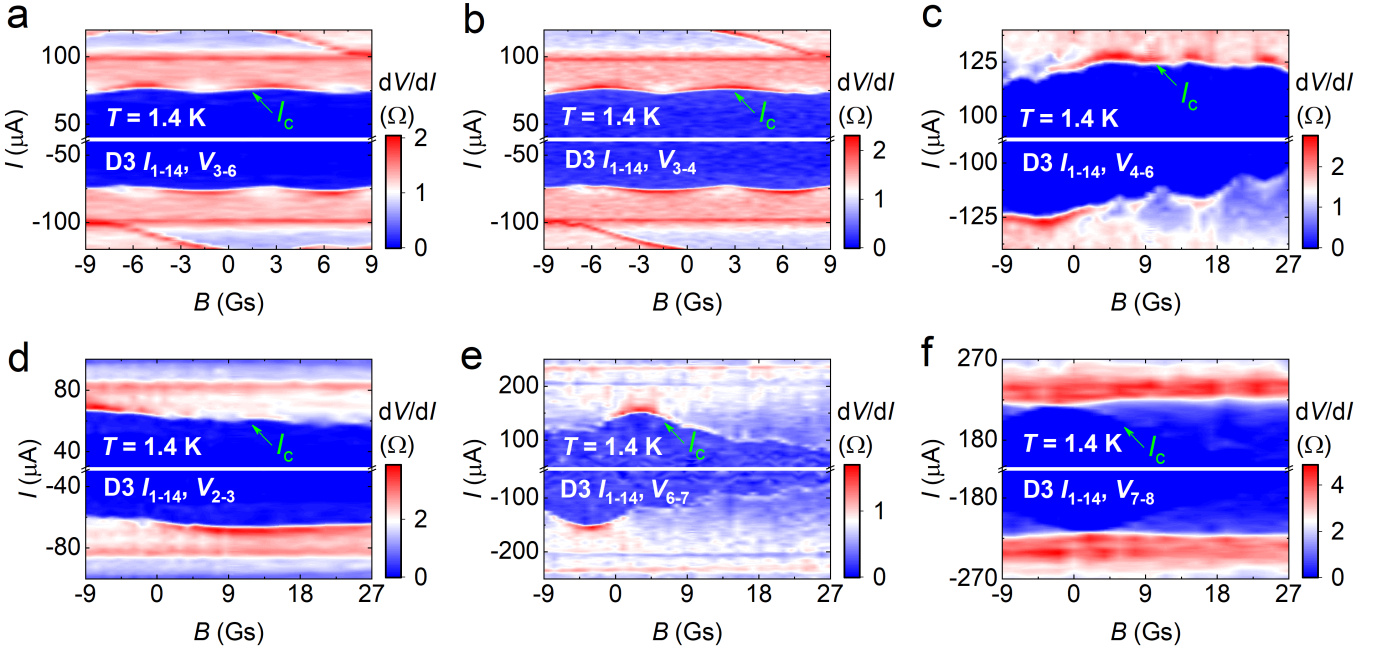
Extended Data Fig. 4. **Multi-step SC phase transitions on dV/dI versus I for D2 measured at different terminals.** **a**, Optical image of D2. All the terminals are numbered (1-8), where 1 and 8 are for current and others are for voltage. **b**, dV/dI versus I at various terminals. Characteristics of dV/dI exhibit notable distinctions across different terminals, including the variation of I_c . Only V_{3-4} displays an apparent SDE. Note that the SDE at V_{6-7} can be excited by thermal cycling, as shown in Extended Data Fig. 2g-i. Given the ultra-high quality of CsV_3Sb_5 single crystals, mild device fabrication processes and the dynamic features on dV/dI , the multi-step transitions and the variation of I_c cannot be simply attributed to significant sample inhomogeneity, but rather implies the formation of SC domain structure (See more discussion in Methods). I_c is influenced by the strength of inter-domain connections.



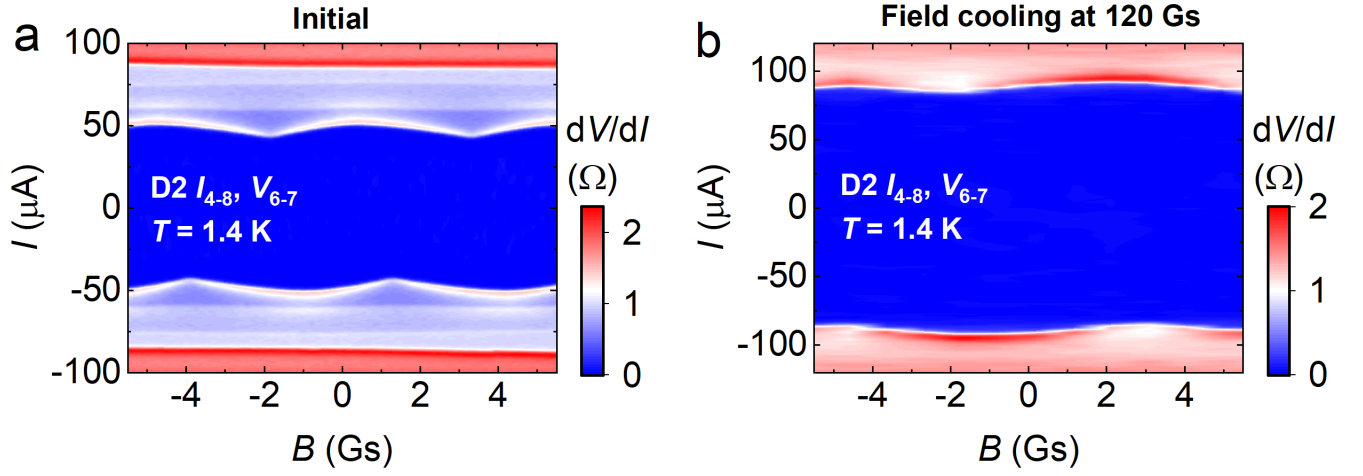
Extended Data Fig. 5. **SIPs for D1, D2 and D3 in a broader range of B .** **a and b**, SIPs for D1, covering the B range of 20 Gs and 240 Gs, respectively, as the Extended Data of Fig. 2a. In **a**, three SIPs (I_c , I'_c and I''_c) are clearly resolved, corresponding to those in Fig. 2a. **b** displays more complex, periodic-like structures, alongside I_c , I'_c and I''_c . Notably, we observe periodic oscillations on I_c . The magnitude of I_c remains nearly unchanged in B up to 240 Gs, as expected from the LP effect. In contrast, I'_c displays a broad Fraunhofer-like pattern, on top of which is a rapid double-slit periodic oscillation. The broad feature is likely associated with a local Josephson junction between neighboring domains (domain bulk contribution) and the rapid mode arises from the LP effect from the domain edge. It implies a composite contribution from the bulk Josephson supercurrent and the edge supercurrent. Relevant discussion is also presented in the main text and Supplementary Note 4, 5. As discussed in Methods, such sharp double-slit SIPs are difficult to explain by alternative interpretations involving chiral charge orders or significant inhomogeneity with the absence of edge supercurrents. **c and d**, SIPs for D2, covering the B range of 40 Gs and 240 Gs, respectively. An explicit periodic oscillation appears on I_c , along with some vague patterns. At $B > 10$ Gs, distinct spikes (marked by white arrows) emerge on I_c , disrupting the periodic patterns, which is the result of the penetration of magnetic vortices into the domain bulk. **e and f**, SIPs for D3, covering the B range of 40 Gs and 240 Gs, respectively. The inset of **e** is the optical image of D3. All the terminals are numbered (1-14).



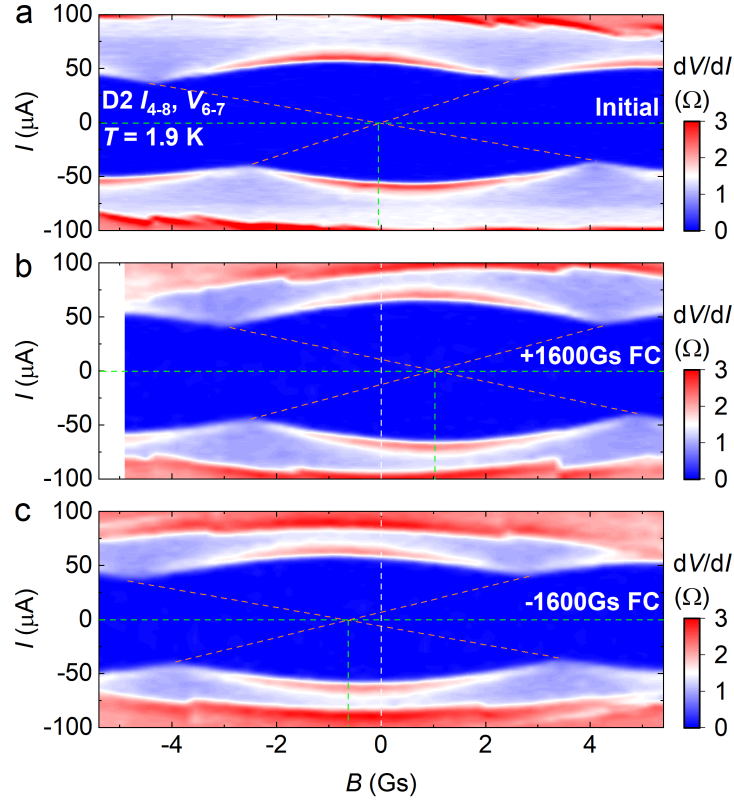
Extended Data Fig. 6. **SIPs for D2 and D3 with the current bias applied between different terminals.** **a**, SIPs for D2 measured at V_{6-7} with current injected into I_{5-8} , which is compared with the data in Fig. 2c (D2, V_{6-7} and I_{4-8}). **b-f**, SIPs for D3 measured at V_{3-6} , but with different current terminals. The oscillation patterns on I_c is nearly unchanged when the current terminals are varied, indicating that the SIPs are associated with the domain structure between the voltage electrodes.



Extended Data Fig. 7. **SIPs for D3 collected at different voltage terminals.** **a-f**, SIPs measured by varying the voltage terminals while applying the current bias on I_{1-14} . Explicit periodic oscillation patterns are observed in V_{3-6} (**a**) and V_{3-4} (**b**). However, the oscillation patterns are vague in V_{4-6} (**c**), V_{2-3} (**d**), V_{6-7} (**e**) and V_{7-8} (**f**). In close inspection of **a**, **b** and **c**, we find that the patterns in V_{3-6} appear to be the superposition of V_{3-4} and V_{4-6} . And the dominant contribution to the SIP (I_c) comes from V_{3-4} . These observations strongly suggest that the SIP arises from a proper domain structure between terminals 3 and 4.



Extended Data Fig. 8. **Field modulation of SIPs for D2 measured at 1.4 K.** **a**, Initial SIP. **b**, SIP measured after field-cooling (FC) from T slightly above T_c at $B = 120$ Gs. After FC, the oscillation patterns underwent significant modifications, including the alteration of period and the increase of $|I_c|$. The patterns roughly returned to their initial state after subsequent multiple thermal cycling from T above T_c . This observation is distinct from what is observed for the same device but measured at different times, as shown in Extended Data Fig. 9. Relevant discussion is presented in Supplementary Note 8.



Extended Data Fig. 9. **Field modulation of SIPs for D2 measured at 1.9 K at different times.** **a**, Initial SIP. **b**, SIP measured after FC from T slightly above T_c at $B = 1600$ Gs. **c**, SIP measured after FC from T slightly above T_c at $B = -1600$ Gs. Note that the period of the initial pattern is distinct from that in Extended Data Fig. 8, which is due to the effect of thermal cycling from 300 K, as referring to Fig. 4d. Remarkably, the oscillation pattern remains nearly unchanged after FC with B even up to 1600 Gs, a feature distinct from that observed in Extended Data Fig. 8. On closer inspection, we discern a peculiar 'advanced' nature of hysteresis in comparing the patterns among the initial, FC 1600 Gs, and FC -1600 Gs curves, i.e. the zero flux line (vertical green dashed line) shifts to positive (negative) B after FC at positive (negative) field. A comprehensive discussion in Supplementary Note 8 argues that the remarkable features in Extended Data Fig. 8, 9 potentially result from chiral SC domain dynamics in response to external B .